Linear and Nonlinear Properties of a Compact High-Kinetic-Inductance WSi Multimode Resonator

Naftali Kirsh[*], Elisha Svetitsky, Samuel Goldstein, Guy Pardo, Ori Hachmo, and Nadav Katz

Racah Institute of Physics, the Hebrew University of Jerusalem, Jerusalem 91904, Israel

The kinetic inductance (KI) of superconducting devices can be exploited for reducing the footprint of linear elements as well as for introducing nonlinearity to the circuit. We characterize the linear and nonlinear properties of a multimode resonator fabricated from amorphous tungsten silicide (WSi), with a fundamental frequency of $f_1 = 172$ MHz. We show how the multimode structure of the device can be used to extract the different quality factors and to aid the nonlinear characterization. In the linear regime, the footprint is reduced by a factor of approximately 2.9 with standard lateral dimensions, with no significant degradation of the internal quality factor compared to a similar Al device. In the nonlinear regime, we observe self-positive frequency shifts at low powers, which can be attributed to saturation of tunneling two-level systems. The cross-mode nonlinearities are described well by a Kerr model with a self-Kerr coefficient on the order of $|K_{11}|/2\pi \approx 1.5 \times 10^{-7}$ Hz per photon. These properties, together with a reproducible fabrication process, make WSi a promising candidate for creating linear and nonlinear circuit quantum electrodynamics elements.

I. INTRODUCTION

The increasing complexity of superconducting circuits [1,2] requires miniaturization of the circuit elements. For resonators used for qubit readout [3], coupling [2,4], and as Purcell filters [5], this can be done by increasing the inductance. A promising direction is the usage of high-kinetic-inductance (high-KI) materials. Kinetic inductance is at the heart of various types of kinetic inductance detectors (KIDs) [6–8]. In addition, linear high-kinetic inductance can also be used to produce high-impedance superinductors [9]. Furthermore, the kinetic inductance of superconducting thin films depends nonlinearly on the circulating current according to:

$$L_k = L_{k,\text{lin.}} \left(1 + \left(\frac{I}{I_*} \right)^2 \right), \qquad (1)$$

where I_* is of the order of the critical current [10,11]. This nonlinearity can be exploited for applications such as traveling-wave amplifiers [12–14] and even qubits [15]. Several high-KI materials have been employed, such as granular Al [16,17], disordered Al [18], NbN [19,20] and TiN [21].

Here, we use amorphous tungsten silicide (WSi) as a high-KI material. WSi is an amorphous superconductor in which T_c and the normal-state resistance can be controlled

by the amount of silicon doping and thickness [22–25]. WSi has been used for single-photon detection due to its structural homogeneity and large hot-spot size [25,26]. The usage of WSi for microwave [23] and thermal KIDs [8] in the x-ray regime has also been investigated. Here, we demonstrate a compact multimode resonator made of a WSi film. In addition to the reduction of footprint due to the linear kinetic inductance, the nonlinearity of the device results in an intermode coupling, which we use as an aid for the device characterization. Our device has low loss and, as shown below, can be used in both the linear and nonlinear regimes. The fabrication method is reproducible and has also been used to create a traveling-wave amplifier [14], compact microwave photonics networks [27], and standard notch-type resonators (see the Supplemental Material [28]). In order to isolate the effects of the kinetic inductance from the geometrical inductance, we also fabricate an Al device with identical geometrical dimensions (except for the thickness of the metal). Since the capacitance and magnetic (geometrical) inductance depend almost only on the geometry and the substrate dielectric constant [29], they should be identical for both devices.

II. FABRICATION

Thin films of WSi are deposited via dc magnetron sputtering. WSi sputter targets are commercially available and we use a $W_{0.55}Si_{0.45}$ target with a 2-in. diameter, supplied by Kurt J. Lesker. WSi is a poor conductor and utilizing

*naftali.kirsh@mail.huji.ac.il

044017-1

sputter settings similar to those for Al and Nb processes heats the target to the point of melting the indium bonds on its back side. We find that target heating is mitigated by using a low sputtering power of 42 W and a resulting deposition rate of 5 nm/min.

We deposit 30 nm of WSi on a high-resistivity ($\rho > 10^4 \, \Omega$ cm) Si substrate. A meandered coplanar waveguide resonator of length 11.6 cm, central strip width 8 μm, and a spacing to ground of 5 μm is defined via optical lithography. The resonator is capacitively coupled to a feed line at either end, with an interdigitated capacitance with four fingers, each of which is 50 μm long (see Fig. 1). The exposed WSi is removed with a tungsten etchant supplied by Sigma Aldrich, with an etch rate of approximately 2–3 nm/s at room temperature. The etchant does not attack PMMA and is therefore also compatible with electron-beam-lithography processes. An identical resonator is fabricated with a film of 80-nm Al. Figure 1(c) shows SEM images of the surface of a 30-nm WSi film, revealing a weakly observable graininess on the order of 10 nm. The insignificance of the grains enables patterning of approximately 0.25–0.5 μm nanowires from sputtered WSi films in which the KI agrees well with the geometric scaling [27].

The devices are mounted in their respective holders and bolted to the base plate of a dilution refrigerator, where they are measured at a base temperature of 20 mK. Linear characterization is done using a vector network analyzer. For the nonlinear mode coupling measurements, we combine the network-analyzer probe signal with a continuous-wave tone from a microwave signal generator.

III. LINEAR CHARACTERIZATION

A. Kinetic inductance fraction and footprint reduction

Our devices are two geometrically identical 11.6-cm-long meandered coplanar waveguides terminated at both ends by interdigitated capacitors, one made of standard Al and the other from WSi as described above. As can be seen in Fig. 2(b), the $\lambda/2$ boundary conditions result in a transmission spectrum of equally spaced peaks at integer multiples of the fundamental frequency $f_1 \equiv \tilde{c}/2l$, where $\tilde{c} = (L_l C_l)^{-1/2}$ is the phase velocity of wave propagation along the waveguide, with L_l (C_l) the inductance (capacitance) per unit length and l the length of the resonator [29]. Figure 2(a) shows linear fits with the function $f_n^{\mathrm{Al,WSi}} = f_1^{\mathrm{Al,WSi}} n$, from which we extract the fundamental frequencies. Using the frequencies of both devices and neglecting the kinetic inductance of the Al [30], we can obtain the kinetic inductance fraction of the WSi device,

$$\alpha \equiv \frac{L_k}{L_k + L_g} = 1 - \frac{L_g}{L_k + L_g} = 1 - \left(\frac{f_1^{\mathrm{WSi}}}{f_1^{\mathrm{Al}}}\right)^2, \quad (2)$$

where the fact that the geometrically dependent capacitance is identical for both devices is used. The fits yield $f_1^{\mathrm{Al}} \approx 499$ MHz and $f_1^{\mathrm{WSi}} \approx 172$ MHz, from which we obtain $\alpha = 0.88 \, (0.02)$ or, equivalently, $L_k \approx 7.3 L_g$. Since the required length for a given fundamental frequency is $l = \tilde{c}/2f_1$, the reduction of length in our case is by a factor of $\sqrt{1-\alpha} \approx 0.35$, i.e., the footprint is smaller by approximately 2.9. Transport measurements of our WSi films
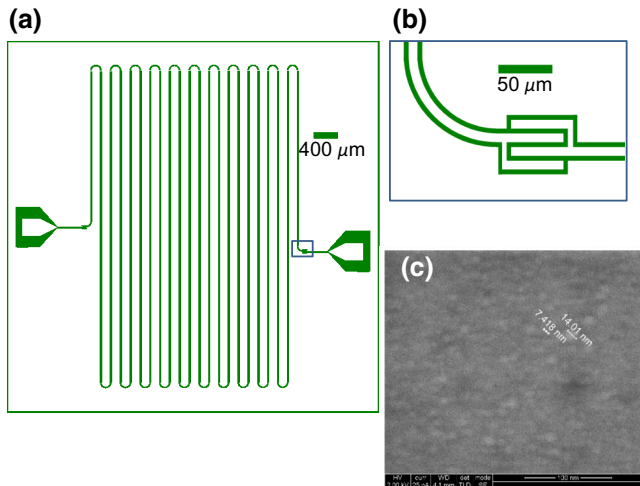

FIG. 1. The multimode resonator device. (a),(b) A sketch of the device: (b) shows the coupling to the feed line via an interdigitated capacitor—white, metal trace and ground; green, exposed Si substrate. (c) A SEM image of the surface of a sputtered 30-nm WSi film: grains of order 10 nm are visible.
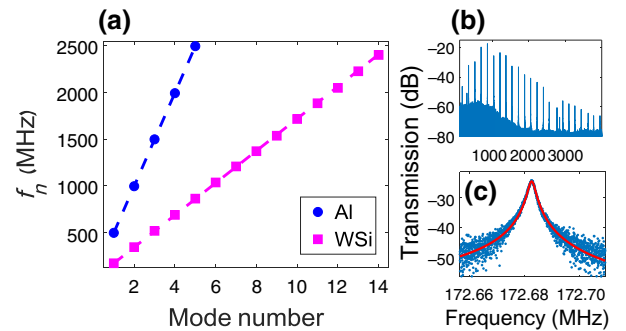

FIG. 2. Reduction of the footprint of the multimode resonator. (a) Multimode spectra of two geometrically identical Al and WSi multimode resonators. The lines are linear fits for the frequencies of the modes. The WSi device obtains a frequency spacing that is smaller by a factor of approximately 2.9 from the Al device using the same length. (b) The raw transmission spectrum of the WSi device, showing the first 23 modes. The profile is affected by the frequency response of the amplifiers. The lower peaks at 300 and 2844 MHz are probably an electronic feed-through and a slot mode. (c) The magnitude of typical transmission data around resonance. The red line is the magnitude of the fit to the complex data [32,33].

give $R \approx 98 \; \Omega/\square$ and $T_c \approx 4.75$ K (see the Supplemental Material [28]) which, assuming a BCS superconductor, yields [31] $L_k \approx 0.03$ nH/$\square$, in agreement with the extracted α (see the Supplemental Material [28]).

B. Quality factors

We next turn to characterizing the internal losses of the devices. The loaded quality factors Q_L of the different modes are fitted from the complex transmission data using standard methods [32,33]. Since for our geometry the off-resonance transmission should ideally vanish, we cannot use it for normalization, as done with notch-type resonators [33]. Instead, we use the fact that the peak transmission in our case satisfies $S_{21}^{\max} = (Q_L/Q_c)$, where Q_c is the coupling quality factor [29]. We note that the coupling quality factor should depend on the mode number n according to [32]

$$Q_c = \frac{n\pi}{4Z_0 Z_L (\omega_n C_c)^2} = \frac{\pi}{4nZ_0 Z_L (\omega_1 C_c)^2} \equiv \frac{Q_{c,1}}{n}, \quad (3)$$

where C_c is the mode-independent coupling capacitance, $Z_L = \sqrt{(L_l/C_l)}$ is the resonator characteristic impedance, and Z_0 is the line characteristic impedance approximated to 50 Ω, neglecting the short WSi feed line. This requires careful calibration of the data, since the transmission of the measurement line is frequency dependent [see Fig. 2(b)]. We perform this calibration by shorting the input and output lines using a standard SMA cable. In order to compensate for uncertainties in this method, we do not use the raw value $Q_c = S_{21}^{\max} Q_L$ but, instead, we fit to Eq. (3), resulting in $Q_{c,1}^{Al} = 2(0.36) \times 10^5$ for Al, which agrees with the geometry of the design, and $Q_{c,1}^{WSi} = 6.2(0.54) \times 10^5$ for WSi [see Fig. 3(a)]. From Eqs. (3) and (2), we can obtain $(Q_{c,1}^{WSi}/Q_{c,1}^{Al}) = \sqrt{L_g/(L_g + L_k)} \left(f_1^{Al}/f_1^{WSi}\right)^2 = (1/\sqrt{1-\alpha}) = 2.9(0.2)$, which agrees with the ratio of the extracted values. Using the values of Q_c, we can extract the internal quality factors as $Q_i^{-1} = Q_L^{-1} - Q_c^{-1}$. The results are shown in Fig. 3(b) for a probe power of approximately -83 dBm. The dominant loss mechanism for superconducting resonators at low temperature is via tunneling two-level systems (TLSs), which can dissipate energy from the electric field to phonons or quasiparticles [34–36]. In this model, the expected temperature dependence of the internal quality factor due to TLSs saturation is [37,38]

$$\frac{1}{Q_i} = \frac{1}{Q_i^0} \tanh\left(\frac{\hbar\omega_n}{2k_B T}\right), \quad (4)$$

where Q_i^0 is the low-temperature weak-field internal quality factor. As can be seen in Fig. 3(b), the behavior of the Al device is well fitted by the theory, while for the WSi device, it seems that Q_i hardly changes with frequency
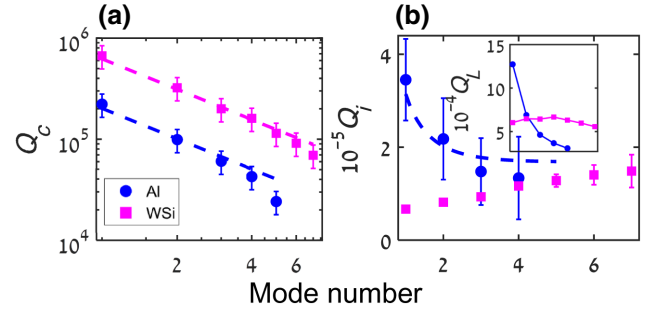

FIG. 3. The quality factors of the devices for different modes. (a) The coupling quality factors for the Al (blue) and WSi (magenta) devices (log-log plot). The dashed lines are fits for the expected $1/n$ dependence, given in Eq. (3). (b) The extracted internal factors for the Al (blue) and WSi (magenta) devices. Q_i is lower for the WSi device probably because a larger fraction of the field energy is stored in the oxides on the surfaces. The dashed line is a fit to a model of thermal saturation of loss-inducing tunneling two-level systems, given in Eq. (4). The lower internal Q at low modes for the WSi device is unexpected and might be a result of coupling to unwanted slot modes [see Fig. 2(b)]. The inset in (b) shows the loaded (total) quality factor, which is dominated by internal loss (coupling) for the WSi (Al) device. The lines are guides to the eye.

or even tends to increase at high frequencies. This might imply that other temperature-independent loss mechanisms exist for this device but it might also be a result of coupling to a slot mode at low frequencies [see Fig. 2(b)]. Comparing modes that are close in frequency we have, for the second mode of the Al device, $Q_{i,2}^{Al} = 2.2(0.9) \times 10^5$, while for the sixth mode of the WSi device we have $Q_{i,6}^{WSi} = 1.4(0.2) \times 10^5$. This minor degradation of the quality factor is to be expected when the geometrical dimensions are smaller, since a larger fraction of the field energy is stored in the oxides on the surfaces, which contain the tunneling TLSs [39]. The noise properties of a traveling-wave amplifier fabricated from WSi (with an additional amorphous Si layer) are measured to be close to the quantum limit [14], indicating that TLSs at the oxide layers of WSi do not contribute unusually to the noise characteristics of the device. We note that since the stored energy depends on the integral of the electric field $\mathbf{e}$ over the volume V as $E_{\text{stored}} = N\hbar\omega_i \propto \int_V |\mathbf{e}|^2 dV$, the relatively low resonance frequencies and long device result in electric field strengths that might not fully saturate the TLSs even at high photon numbers. Additional surface treatment may further reduce the loss.

IV. NONLINEAR CHARACTERIZATION

A. Self-nonlinearity

As described in Eq. (1), at high powers the kinetic inductance has a nonlinear dependence on current. This dependence results in a shift of the resonance frequency,

which is linear in the stored energy, i.e., a Kerr nonlinearity [40]. We can approximate the shift of mode n in the limit of a small nonlinear inductance as

$$\Delta f_n = \frac{n}{2\sqrt{C\left(L_{\text{lin.}} + L_{nl}\right)}} - \frac{n}{2\sqrt{L_{\text{lin.}}C}}$$

$$\approx -\frac{1}{2}\frac{n}{2\sqrt{L_{\text{lin.}}C}}\frac{L_k}{L_{\text{lin.}}}\left(\frac{I}{I_*}\right)^2 = -\frac{1}{2}f_n\frac{L_k}{L_{\text{lin.}}}\left(\frac{I}{I_*}\right)^2. \tag{5}$$

If we now assume that current circulates due to energy stored in the pumped mode m (possibly with $m = n$) with an average number of photons $\langle N\rangle_m = (LI^2/\hbar\omega_m)$, we obtain

$$2\pi\Delta f_n \equiv \Delta\omega_n \approx -\pi\frac{L_k}{L_{\text{lin.}}^2 I_*^2}\hbar\omega_n\omega_m\langle N\rangle_m \equiv K_{nm}\langle N\rangle_m. \tag{6}$$

where K_{nm} is termed the self-Kerr (cross-Kerr) coefficient for the case $n = m$ ($n \neq m$) [41]. Note that $K_{nm} = K_{11}nm$ for the case of a linear mode structure. Physically, this is a result of the linear dependence of the pumping photon energy and the shifted resonance frequency on the mode number. We measure the self-frequency shifts by varying the power of the probe field and measuring the resonance frequency shift for the different modes. The results of measurements from two different cool-downs are shown in Fig. 4. At high pump powers, the frequency shift is indeed negative and seems to be linear in both stored energy and mode number (see inset in Fig. 4), in agreement with Eq. (6). Interestingly, at low energies we observe a *positive* frequency shift when increasing the power, which is incompatible with the standard model of nonlinear kinetic inductance, given in Eq. (1). The positive shift is more pronounced at the first cool-down but is also observed at the second cool-down. The only known mechanisms for a positive frequency shift when using a single-probe tone are broadband heating of the tunneling TLSs to temperatures of $T \gtrsim 0.45(\hbar\omega/k_B)$ [37] or depopulation of thermal quasiparticle states by the microwave field [42,43]. Since the last mechanism is relevant only at high temperatures $T \gtrsim 0.5T_c$, it seems to be irrelevant. Furthermore, since for our device $(\hbar\omega_1/k_B) = 8$ mK, TLSs heating seems plausible. Another hint pointing in that direction is that it has recently been reported [7] that WSi has an anomalously high heat capacity at low temperatures, i.e., it may stay hot after it is heated by the radiation. We note that in addition to the weaker positive shift, at the second cool-down the quality factors are slightly higher than in the first. This might support the hypothesis of TLSs causing the shifts, since a new TLSs distribution is generated upon thermal cycling the cryostat [44], which might also reduce the loss. However, the positive shifts are not observed in cross-Kerr
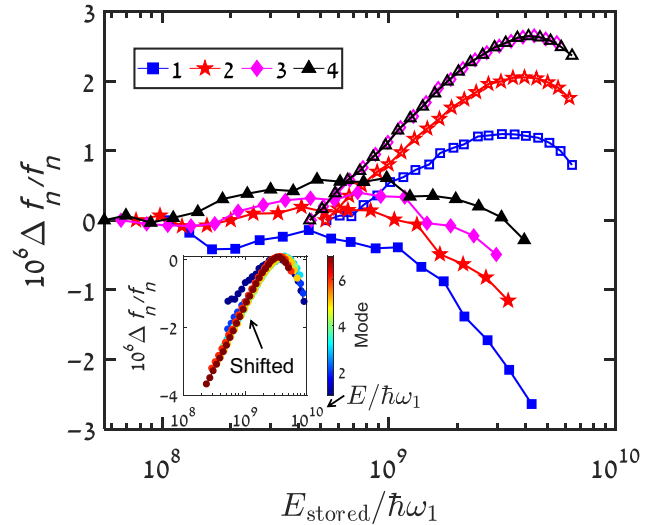

FIG. 4. Self-nonlinearity frequency shifts. The differential frequency shift for the first four modes (denoted by different marker shapes as detailed in the legend) of the WSi device as a function of the stored energy (in units of first-mode photons) for two different cool-downs. The empty (full) markers are measurements from the first (second) cool-down. The lines are guides to the eye. The inset shows the (vertically shifted) frequency shifts of the first seven modes, measured at the first cool-down. The positive frequency shifts hinder the evaluation of the bare self-Kerr coefficients.

experiments (Fig. 5, see below), implying a resonant effect and not a broadband heating. Another contradiction compared to a broadband heating model is the fact that the slope of the positive shift is *larger* for the higher modes, for which $(k_B T/\hbar\omega_n)$ is *smaller*. While frequency shifts resulting from a separate detuned strong pump tone has been observed and explained as a consequence of asymmetric saturation of off-resonant TLSs [45,46], a single probe should result in symmetric saturation, with no net frequency shift. The effect cannot be explained by a random asymmetry of TLSs frequencies due to their finite number [45,46] because the direction of the shift is positive for all probed modes. We note that positive shifts are also observed by us for devices with resonance frequencies of approximately 6–7 GHz, for which the temperature scale is much higher (see the Supplemental Material [28]). In addition, a positive frequency shift has also been shown in the data of the high-KI NbN resonator reported in Ref. [20], for which the resonance frequency is approximately 6.8 GHz. In Ref. [21], a positive shift in an approximately 1-GHz TiN resonator is attributed to TLSs effects. Broadband heating of TLSs is used to explain the positive frequency shifts of four harmonics of an approximately 2.14-GHz Nb resonator in Ref. [47]. Further investigation of this effect is needed. Nevertheless, the presence of the positive frequency shift hinders the extraction of the bare self-Kerr coefficient.
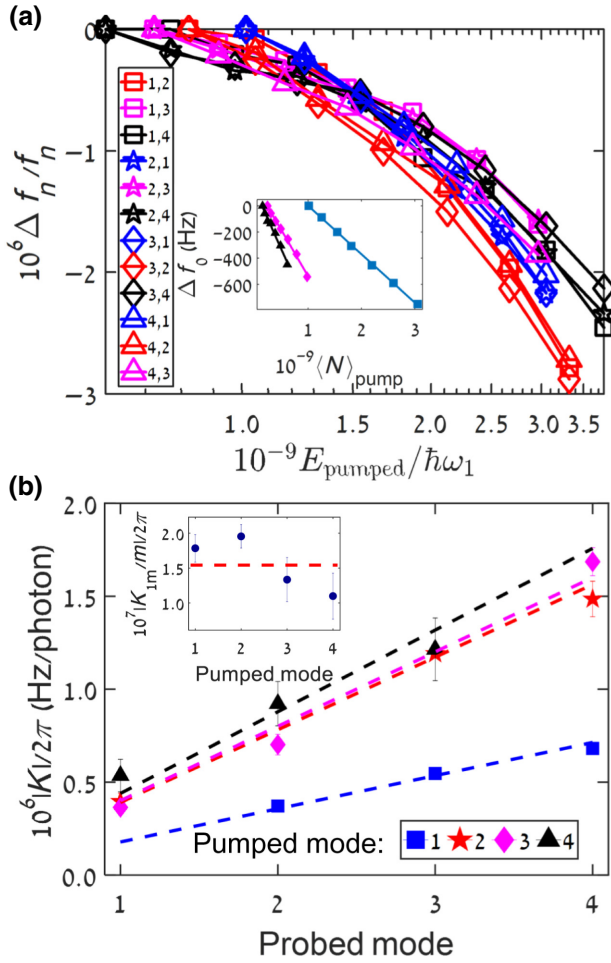
(a)

(b)

FIG. 5. Cross-Kerr frequency shifts. (a) The differential frequency shift for different modes of the WSi device as a function of the stored energy in various pumped modes (in units of first-mode photons). In the legend, (n,m) denotes (probed mode n, pumped mode m). The inset shows linear fits to the frequency shifts of the second mode. (b) The extracted cross-Kerr coefficients K_{nm} when pumping mode m as a function of the probed mode n. The dashed lines are fits to $K_{nm} \propto K_{1m}n$. The inset shows the fitted K_{1m} divided by the pumped mode number m as a function of m, which should equal K_{11}. The dashed line is the average of K_{1m}/m.

B. Cross-Kerr nonlinearity and mode coupling

In addition to the self-Kerr effects, in the second cooldown we also investigate the nonlinear shifts of a probed mode n when another mode m is strongly pumped. This is done by pumping at a constant frequency (the low-power resonance f_m) with various powers, while probing weakly around f_n in order to extract the frequency shift Δf_n. Since the resonance frequency of the pumped mode is shifted according to its own self-nonlinearity effects and its quality factor also changes, the stored energy E_{pumped} is not linear with the injected power. Therefore, we need to calculate E_{pumped} using the power-dependent quality factors and

resonance frequencies extracted in the self-nonlinearity measurements. The results are shown in Fig. 5(a). As expected from Eq. (6), the differential shifts approximately coincide. Fitting the extracted cross-Kerr parameters for each pumped (probed) mode m (n) to $K_{nm} = K_{1m}n$ [see Fig. 5(b)], we obtain K_{1m} for the first four modes. From the average of K_{1m}/m, we estimate $K_{11}/2\pi = -1.5(0.1) \times 10^{-7}$ Hz per photon, which corresponds to $I_* \approx 29$ mA, in agreement with the transport measurements (see the Supplemental Material [28]). The variability of K_{1m}/m may be a result of the different overlaps of the spatial-mode functions with local hot spots, which causes an effective mode-dependent I_*, or may be due to uncertainty in the calculation of E_{pumped}.

V. SUMMARY

In conclusion, we demonstrate the use of WSi as a high-KI material for both decreasing the footprint of a multimode resonator and introducing both intermode and intramode nonlinearities to the device. The fabrication is straightforward and reproducible and yields a reduction of the footprint by a factor of approximately 2.9 with standard lateral dimensions. At high powers, we observe nonlinear behavior, with a Kerr coefficient on the order of $|K_{11}|/2\pi \approx 1.5 \times 10^{-7}$ Hz per photon for the first mode (172 MHz). Further reduction of the footprint requires making α closer to 1. Since $L_K \propto R$ for $T \ll T_c$, where R is the normal resistance [31], this can be accomplished by a reduction of the cross section. Note that L_g can be kept constant if the ratio between the central strip width and the spacing to ground does not change [29]. As can be seen from Eq. (6), this also increases the magnitude of the Kerr coefficient. In addition, the Kerr coefficient can be increased by raising the fundamental frequency, since $f_1 \sim (1/\sqrt{L_{\text{tot}}})$ and therefore $K_{11} \propto (f_1)^4$ at the limit of $\alpha \approx 1$ of Eq. (6). The footprint of the device can also be reduced independently from the nonlinearity by increasing its capacitance at the cost of a larger loss but with an impedance closer to 50 Ω as demonstrated recently with hybrid Al-WSi devices [14,27]. In this paper, we use the nonlinear mode coupling for device characterization but it may also be used for other purposes, such as measurement of one mode by monitoring another one [48,49] or even two-mode squeezing [50] if the coupling is sufficiently strong when compared with losses.

[1] F. Arute, K. Arya, R. Babbush, D. Bacon, J. C. Bardin, R. Barends, R. Biswas, S. Boixo, F. G. Brandao, and

D. A. Buell *et al.*, Quantum supremacy using a pro-grammable superconducting processor, Nature **574,** 505 (2019).

[2] P. Jurcevic, A. Javadi-Abhari, L. S. Bishop, I. Lauer, D. Borgorin, M. Brink, L. Capelluto, O. Gunluk, T. Itoko, and N. Kanazawa *et al.*, Demonstration of quantum volume 64 on a superconducting quantum computing system, Quantum Science and Technology (2021).

[3] A. Blais, R. S. Huang, A. Wallraff, S. M. Girvin, and R. J. Schoelkopf, Cavity quantum electrodynamics for superconducting electrical circuits: An architecture for quantum computation, Phys. Rev. A—At. Mol. Opt. Phys. **69,** 062320 (2004).

[4] J. Majer, J. Chow, J. Gambetta, J. Koch, B. Johnson, J. Schreier, L. Frunzio, D. Schuster, A. A. Houck, and A. Wallraff *et al.*, Coupling superconducting qubits via a cavity bus, Nature **449,** 443 (2007).

[5] M. D. Reed, B. R. Johnson, A. A. Houck, L. DiCarlo, J. M. Chow, D. I. Schuster, L. Frunzio, and R. J. Schoelkopf, Fast reset and suppressing spontaneous emission of a superconducting qubit, Appl. Phys. Lett. **96,** 203110 (2010).

[6] P. K. Day, H. G. LeDuc, B. A. Mazin, A. Vayonakis, and J. Zmuidzinas, A broadband superconducting detector suitable for use in large arrays, Nature **425,** 817 (2003).

[7] B. A. Mazin, Superconducting materials for microwave kinetic inductance detectors, arXiv:2004.14576 (2020).

[8] O. Quaranta, T. W. Cecil, L. Gades, B. Mazin, and A. Miceli, X-ray photon detection using superconducting resonators in thermal quasi-equilibrium, Supercond. Sci. Technol. 26, 105021 (2013), arXiv:1304.3387.

[9] P. Kamenov, W.-S. Lu, K. Kalashnikov, T. DiNapoli, M. T. Bell, and M. E. Gershenson, Granular Aluminum Meandered Superinductors for Quantum Circuits, Phys. Rev. Appl. **13,** 054051 (2020).

[10] J. Zmuidzinas, Superconducting microresonators: Physics and applications, Annu. Rev. Condens. Matter Phys. **3,** 169 (2012).

[11] A. V. Semenov, I. A. Devyatov, M. P. Westig, and T. M. Klapwijk, Effect of Microwaves on Superconductors for Kinetic Inductance Detection and Parametric Amplification, Phys. Rev. Appl. **13,** 024079 (2020).

[12] M. R. Vissers, R. P. Erickson, H.-S. Ku, L. Vale, X. Wu, G. Hilton, and D. P. Pappas, Low-noise kinetic inductance traveling-wave amplifier using three-wave mixing, Appl. Phys. Lett. **108,** 012601 (2016).

[13] M. Malnou, M. Vissers, J. Wheeler, J. Aumentado, J. Hubmayr, J. Ullom, and J. Gao, Three-wave mixing kinetic inductance traveling-wave amplifier with near-quantum-limited noise performance, PRX Quantum **2,** 010302 (2021).

[14] S. Goldstein, N. Kirsh, E. Svetitsky, Y. Zamir, O. Hachmo, C. E. M. de Oliveira, and N. Katz, Four wave-mixing in a microstrip kinetic inductance travelling wave parametric amplifier, Appl. Phys. Lett. **116,** 152602 (2020).

[15] P. Winkel, K. Borisov, L. Grünhaupt, D. Rieger, M. Spiecker, F. Valenti, A. V. Ustinov, W. Wernsdorfer, and I. M. Pop, Implementation of a Transmon Qubit Using Superconducting Granular Aluminum, Phys. Rev. X **10,** 031032 (2020).

[16] L. Grünhaupt, N. Maleeva, S. T. Skacel, M. Calvo, F. Levy-Bertrand, A. V. Ustinov, H. Rotzinger, A. Monfardini,

G. Catelani, and I. M. Pop, Loss Mechanisms and Quasiparticle Dynamics in Superconducting Microwave Resonators Made of Thin-Film Granular Aluminum, Phys. Rev. Lett. **121,** 117001 (2018).

[17] H. Rotzinger, S. Skacel, M. Pfirrmann, J. Voss, J. Münzberg, S. Probst, P. Bushev, M. Weides, A. Ustinov, and J. Mooij, Aluminium-oxide wires for superconducting high kinetic inductance circuits, Supercond. Sci. Technol. **30,** 025002 (2016).

[18] W. Zhang, K. Kalashnikov, W.-S. Lu, P. Kamenov, T. DiNapoli, and M. Gershenson, Microresonators Fabricated from High-Kinetic-Inductance Aluminum Films, Phys. Rev. Appl. **11,** 011003 (2019).

[19] D. Niepce, J. Burnett, and J. Bylander, High Kinetic Inductance NbN Nanowire Superinductors, Phys. Rev. Appl. **11,** 044014 (2019).

[20] W. Xing-Yu, P. Jia-Zheng, L. Ya-Peng, J. Jun-Liang, L. Zi-Shuo, L. Sheng, T. Xue-Cou, Z. Qing-Yuan, J. Xiao-Qing, and K. Lin *et al.*, Compact NbN resonators with high kinetic inductance, Chinese Physics B (2020).

[21] L. Swenson, P. Day, B. Eom, H. Leduc, N. Llombart, C. McKenney, O. Noroozian, and J. Zmuidzinas, Operation of a titanium nitride superconducting microresonator detector in the nonlinear regime, J. Appl. Phys. **113,** 104501 (2013).

[22] S. Kondo, Superconducting characteristics and the thermal stability of tungsten-based amorphous thin films, J. Mater. Res. **7,** 853 (1992).

[23] T. Cecil, A. Miceli, O. Quaranta, C. Liu, D. Rosenmann, S. McHugh, and B. Mazin, Tungsten silicide films for microwave kinetic inductance detectors, Appl. Phys. Lett. **101,** 032601 (2012).

[24] X. Zhang, A. Engel, Q. Wang, A. Schilling, A. Semenov, M. Sidorova, H.-W. Hübers, I. Charaev, K. Ilin, and M. Siegel, Characteristics of superconducting tungsten silicide $W_x Si_{1-x}$ for single photon detection, Phys. Rev. B **94,** 174509 (2016).

[25] B. Baek, A. E. Lita, V. Verma, and S. W. Nam, Superconducting a-$W_x Si_{1-x}$ nanowire single-photon detector with saturated internal quantum efficiency from visible to 1850 nm, Appl. Phys. Lett. **98,** 251105 (2011).

[26] F. Marsili, V. B. Verma, J. A. Stern, S. Harrington, A. E. Lita, T. Gerrits, I. Vayshenker, B. Baek, M. D. Shaw, R. P. Mirin, and S. W. Nam, Detecting single infrared photons with 93% system efficiency, Nat. Photonics 7, 210 (2013), arXiv:1209.5774.

[27] S. Goldstein, G. Pardo, N. Kirsh, N. Gaiser, C. Padurariu, B. Kubala, J. Ankerhold, and N. Katz, Compact itinerant microwave photonics with superconducting high-kinetic inductance microstrips, arXiv:2106.15951 [physics.app-ph] (2021).

[28] See the Supplemental Material at http://link.aps.org/supplemental/10.1103/PhysRevApplied.16.044017 for transport measurements and measurements of notch-type quarter-wave resonators.

[29] M. Göppl, A. Fragner, M. Baur, R. Bianchetti, S. Filipp, J. M. Fink, P. J. Leek, G. Puebla, L. Steffen, and A. Wallraff, Coplanar waveguide resonators for circuit quantum electrodynamics, J. Appl. Phys. 104, 113904 (2008), arXiv:0807.4094.

[30] J. Gao, J. Zmuidzinas, B. Mazin, P. Day, and H. Leduc, Experimental study of the kinetic inductance fraction

of superconducting coplanar waveguide, Nucl. Instrum. Methods Phys. Res. Sect. A: Accelerators, Spectrometers, Detectors Associated Equipment **559**, 585 (2006).

[31] M. Tinkham, *Introduction to superconductivity* (Dover Corporation, 2004) Chap. 3.10.

[32] B. A. Mazin, Ph.D. thesis, Division of Physics, Mathematics and Astronomy, California Institute of Technology, 2005.

[33] S. Probst, F. B. Song, P. A. Bushev, A. V. Ustinov, and M. Weides, Efficient and robust analysis of complex scattering data under noise in microwave resonators, Rev. Sci. Instrum. **86**, 024706 (2014), arXiv:1410.3365.

[34] W. Phillips, Two-level states in glasses, Rep. Prog. Phys. **50**, 1657 (1987).

[35] J. M. Martinis, K. B. Cooper, R. McDermott, M. Steffen, M. Ansmann, K. Osborn, K. Cicak, S. Oh, D. P. Pappas, and R. W. Simmonds *et al.*, Decoherence in Josephson Qubits from Dielectric Loss, Phys. Rev. Lett. **95**, 210503 (2005).

[36] C. Müller, J. H. Cole, and J. Lisenfeld, Towards understanding two-level-systems in amorphous solids: Insights from quantum circuits, Rep. Prog. Phys. **82**, 124501 (2019).

[37] J. Gao, Ph.D. thesis, Division of Engineering and Applied Science, California Institute of Technology, 2008.

[38] D. P. Pappas, M. R. Vissers, D. S. Wisbey, J. S. Kline, and J. Gao, Two level system loss in superconducting microwave resonators, IEEE Trans. Appl. Supercond. **21**, 871 (2011).

[39] J. Gao, M. Daal, A. Vayonakis, S. Kumar, J. Zmuidzinas, B. Sadoulet, B. a. Mazin, P. K. Day, and H. G. Leduc, Experimental evidence for a surface distribution of two-level systems in superconducting lithographed microwave resonators, Appl. Phys. Lett. **92**, 152505 (2008).

[40] B. Yurke and E. Buks, Performance of cavity-parametric amplifiers, employing Kerr nonlinearites, in the presence of two-photon loss, J. Light. Technol. **24**, 5054 (2006).

[41] N. Maleeva, L. Grünhaupt, T. Klein, F. Levy-Bertrand, O. Dupre, M. Calvo, F. Valenti, P. Winkel, F. Friedrich, and W. Wernsdorfer *et al.*, Circuit quantum electrodynamics of granular aluminum resonators, Nat. Commun. **9**, 1 (2018).

[42] P. De Visser, D. Goldie, P. Diener, S. Withington, J. Baselmans, and T. Klapwijk, Evidence of a Nonequilibrium Distribution of Quasiparticles in the Microwave Response of a Superconducting Aluminum Resonator, Phys. Rev. Lett. **112**, 047004 (2014).

[43] T. Klapwijk and P. de Visser, The discovery, disappearance and re-emergence of radiation-stimulated superconductivity, Ann. Phys. (N. Y.) **0**, 168104 (2020).

[44] Y. Shalibo, Y. Rofe, D. Shwa, F. Zeides, M. Neeley, J. M. Martinis, and N. Katz, Lifetime and Coherence of Two-Level Defects in a Josephson Junction, Phys. Rev. Lett. **105**, 177001 (2010).

[45] N. Kirsh, E. Svetitsky, A. L. Burin, M. Schechter, and N. Katz, Revealing the nonlinear response of a tunneling two-level system ensemble using coupled modes, Phys. Rev. Mater. **1**, 012601 (2017).

[46] T. Capelle, E. Flurin, E. Ivanov, J. Palomo, M. Rosticher, S. Chua, T. Briant, P.-F. Cohadon, A. Heidmann, and T. Jacqmin *et al.*, Probing a Two-Level System Bath via the Frequency Shift of an Off-Resonantly Driven Cavity, Phys. Rev. Appl. **13**, 034022 (2020).

[47] J. M. Sage, V. Bolkhovsky, W. D. Oliver, B. Turek, and P. B. Welander, Study of loss in superconducting coplanar waveguide resonators, J. Appl. Phys. **109**, 063915 (2011).

[48] E. Buks and B. Yurke, Dephasing due to intermode coupling in superconducting stripline resonators, Phys. Rev. A **73**, 023815 (2006).

[49] G. Tancredi, G. Ithier, and P. Meeson, Bifurcation, mode coupling and noise in a nonlinear multimode superconducting microwave resonator, Appl. Phys. Lett. **103**, 063504 (2013).

[50] G. Andersson, S. W. Jolin, M. Scigliuzzo, R. Borgani, M. O. Tholén, D. B. Haviland, and P. Delsing, Squeezing and correlations of multiple modes in a parametric acoustic cavity, arXiv:2007.05826 (2020).